

THE STATISTICS OF SUPERSONIC ISOTHERMAL TURBULENCE

ALEXEI G. KRITSUK¹, MICHAEL L. NORMAN, PAOLO PADOAN, AND RICK WAGNER

Department of Physics and Center for Astrophysics and Space Sciences, University of California, San Diego,
9500 Gilman Drive, La Jolla, CA 92093-0424; akritsuk@ucsd.edu, mlnorman@ucsd.edu, ppadoan@ucsd.edu

ApJ 665, 000–000, 2007 August 20

ABSTRACT

We present results of large-scale three-dimensional simulations of supersonic Euler turbulence with the piecewise parabolic method and multiple grid resolutions up to 2048^3 points. Our numerical experiments describe non-magnetized driven turbulent flows with an isothermal equation of state and an rms Mach number of 6. We discuss numerical resolution issues and demonstrate convergence, in a statistical sense, of the inertial range dynamics in simulations on grids larger than 512^3 points. The simulations allowed us to measure the absolute velocity scaling exponents for the first time. The inertial range velocity scaling in this strongly compressible regime deviates substantially from the incompressible Kolmogorov laws. The slope of the velocity power spectrum, for instance, is -1.95 compared to $-5/3$ in the incompressible case. The exponent of the third-order velocity structure function is 1.28, while in incompressible turbulence it is known to be unity. We propose a natural extension of Kolmogorov’s phenomenology that takes into account compressibility by mixing the velocity and density statistics and preserves the Kolmogorov scaling of the power spectrum and structure functions of the density-weighted velocity $\mathbf{v} \equiv \rho^{1/3}\mathbf{u}$. The low-order statistics of \mathbf{v} appear to be invariant with respect to changes in the Mach number. For instance, at Mach 6 the slope of the power spectrum of \mathbf{v} is -1.69 , and the exponent of the third-order structure function of \mathbf{v} is unity. We also directly measure the mass dimension of the “fractal” density distribution in the inertial subrange, $D_m \approx 2.4$, which is similar to the observed fractal dimension of molecular clouds and agrees well with the cascade phenomenology.

Subject headings: hydrodynamics — instabilities — ISM: structure — methods: numerical — turbulence

1. INTRODUCTION

Understanding the nature of supersonic turbulence is of fundamental importance in both astrophysics and aeronautical engineering. In the interstellar medium (ISM), highly compressible turbulence is believed to control star formation in dense molecular clouds (Padoan & Nordlund 2002). In radiation-driven outflows from carbon-dominant Wolf-Rayet stars, supersonic turbulence creates highly clumpy structure that is stochastically variable on a very short time-scale (e.g., Acker et al. 2002). Finally, a whole class of more *terrestrial* applications deals with the drag and stability of projectiles traveling through the air at hypersonic speeds.

Molecular clouds have an extremely inhomogeneous structure and the intensity of their internal motions corresponds to an rms Mach number of order 20. Larson (1981) has demonstrated that within the range of scales from 0.1 to 100 pc, the gas density and the velocity dispersion tightly correlate with the cloud size.² Supported by other independent observational facts indicating scale invariance, these relationships are often interpreted in terms of supersonic turbulence with characteristic Reynolds numbers $Re \sim 10^8$ (Elmegreen & Scalo 2004). Within a wide range of densities above 10^3 cm^{-3} , the gas temperature remains close to $\approx 10 \text{ K}$, since the thermal equilibration time at these densities is shorter than a typical hydrodynamic (HD) timescale. Thus, an isothermal equation of state can be used as a reasonable approximation. Self-gravity, magnetic fields, chemistry, cooling, and heating, as well as radiative transfer, should ultimately be accounted for in turbulent models of molecular clouds. However, since highly com-

pressible turbulence still remains an unsolved problem even in the absence of magnetic fields, our main focus here is specifically on the more tractable HD aspects of the problem.

Magnetic fields are important for the general ISM dynamics and, particularly, for the star formation process. Observations of molecular clouds are consistent with the presence of super-Alfvénic turbulence (Padoan et al. 2004a), and thus, the average magnetic field strength may be much smaller than required to support the clouds against the gravitational collapse (Padoan & Nordlund 1997, 1999). Even weak fields, however, have the potential to modify the properties of supersonic turbulent flows through the effects of magnetic tension and magnetic pressure and introduce small-scale anisotropies. Magnetic tension tends to stabilize hydrodynamically unstable post-shock shear layers (Miura & Pritchett 1982; Keppens et al. 1999; Ryu et al. 2000; Baty et al. 2003). The shock jump conditions modified by magnetic pressure result in substantially different predictions for the initial mass function of stars forming in non-magnetic and magnetized cases via turbulent fragmentation (Padoan et al. 2007). Remarkably, although not surprisingly (e.g., Armi & Flament 1985), the impact of magnetic field on the low-order statistics of super-Alfvénic turbulence appears to be rather limited. At a grid resolution of 1024^3 points, the slopes of the power spectra in our simulations show stronger sensitivity to the numerical diffusivity of the scheme of choice than to the presence of the magnetic field (Padoan et al. 2007). The similarity of non-magnetized and weakly magnetized turbulence will allow us to compare our HD results with those from super-Alfvénic magnetohydrodynamic (MHD) simulations where equivalent pure HD simulations are not available in the literature.

Numerical simulations of *decaying* supersonic HD turbulence with the piecewise parabolic method (PPM) in

¹ Also at: Sobolev Astronomical Institute, St. Petersburg State University, St. Petersburg, Russia.

² For an earlier version of what is now known as Larson’s relations, see Kaplan & Pronik (1953) and also see Brunt (2003) for the latest results on the velocity dispersion–cloud size relation.

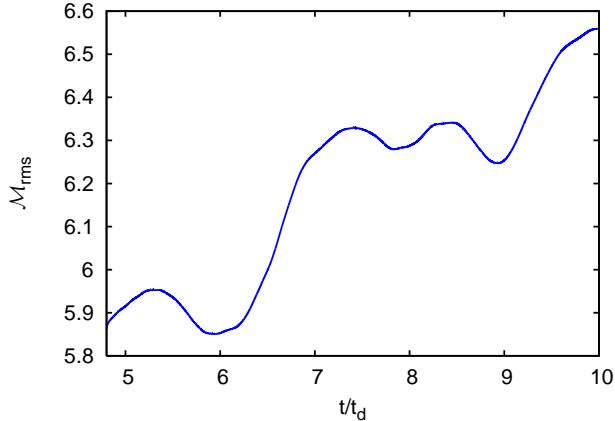


FIG. 1.— Time evolution of the rms Mach number in the 1024^3 simulation of driven Mach 6 turbulence.

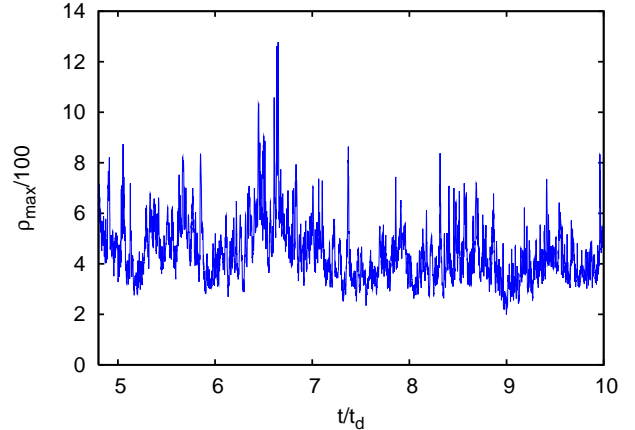


FIG. 2.— Same as Fig. 1, but for the maximum gas density.

two dimensions were pioneered by Passot et al. (1988)³ and then followed up with high-resolution two- and three-dimensional simulations by Porter et al. (1992a,b, 1994, 1998). Sytine et al. (2000) compared the results of PPM Euler computations with PPM Navier-Stokes results and showed that the Euler simulations agree well with the high-Re limit attained in the Navier-Stokes models. The convergence in a statistical sense as well as the direct comparison of structures in configuration space indicate the ability of PPM to accurately simulate turbulent flows over a wide range of scales. More recently, Porter et al. (2002) discussed measures of intermittency in simulated *driven* transonic flows at Mach numbers of the order unity on grids of up to 512^3 points. Porter et al. (1999) review the results of these numerical studies, focusing on the origin and evolution of turbulent structures in physical space as well as on scaling laws for two-point structure functions. One of the important results of this fundamental work is the demonstration of the compatibility of a Kolmogorov-type (Kolmogorov 1941a, K41) spectrum with a *mild* gas compressibility at transonic Mach numbers.

Since most of the computations discussed above assume a perfect gas equation of state with the ratios of specific heats $\gamma = 7/5$ or $5/3$ and Mach numbers generally below 2, the question remains whether this result will still hold for near isothermal conditions and *hypersonic* Mach numbers characteristic of dense parts of star-forming molecular clouds where the gas compressibility is much higher. What kind of coherent structures should one expect to see in highly supersonic turbulence? Do low-order statistics of turbulence follow the K41 predictions closely in this regime? How can the statistical diagnostics traditionally used in studies of incompressible turbulence be extended to reconstruct the energy cascade properties in supersonic flows? How can we measure the intrinsic intermittency of supersonic turbulence? Many of these and similar questions can only be addressed with numerical simulations of sufficiently high resolution. The interpretation of astronomical data from new surveys of the cold ISM and dust in the Milky Way by the *Spitzer* and *Herschel Space Observatory* satellites requires more detailed knowledge of these basic properties of supersonic turbulence.

In this paper we report the results from large-scale numerical simulations of driven supersonic isothermal turbulence at Mach 6 with PPM and grid resolutions up to 2048^3 points.

³ See a review on compressible turbulence by Pouquet et al. (1991) for references to earlier works.

The paper is organized as follows: Section 2 contains the details of the simulations' setup and describes the input parameters. The statistical diagnostics, including power spectra of the velocity, the kinetic energy and the density, and velocity structure functions, together with a discussion of turbulent structures and their fractal dimension are presented in Section 3. In Section 3.9 we combine the scaling laws determined in our numerical experiments to verify a simple compressible cascade model proposed by Fleck (1996). We also introduce a new variable $\mathbf{v} \equiv \rho^{1/3}\mathbf{u}$ that controls the energy transfer rate through the compressible cascade. We then summarize the results and discuss possible ways to validate our numerical model with astrophysical observations in Sections 4 and 5.

2. METHODOLOGY

We use PPM implemented in the *Enzo* code⁴ to solve the Euler equations for the gas density ρ and the velocity \mathbf{u} with a constant external acceleration term $\mathbf{F}(\mathbf{x})$ such that $\langle \mathbf{F}(\mathbf{x}) \rangle = 0$,

$$\partial_t \rho + \nabla \cdot (\rho \mathbf{u}) = 0, \quad (1)$$

$$\partial_t \mathbf{u} + \mathbf{u} \cdot \nabla \mathbf{u} = -\nabla \rho / \rho + \mathbf{F}, \quad (2)$$

in a periodic box of linear size $L = 1$ starting with an initially uniform density distribution $\rho(\mathbf{x}, t = 0) = \rho_0(\mathbf{x}) \equiv 1$ and assuming the sound speed $c \equiv 1$. The equations that were actually numerically integrated were written in a conventional form of conservation laws for the mass, momentum, and total energy that is less compact, but *nearly* equivalent to equations (1) and (2), since in practice we mimic the isothermal equation of state by setting the specific heats ratio in the ideal gas equation of state very close to unity, $\gamma = 1.001$.

The simulations were initialized on grids of 256^3 or 512^3 points with a random velocity field $\mathbf{u}(\mathbf{x}, t = 0) = \mathbf{u}_0(\mathbf{x}) \propto \mathbf{F}$ that contains only large-scale power within the range of wavenumbers $k/k_{min} \in [1, 2]$, where $k_{min} = 2\pi$, and that corresponds to the rms Mach number $\mathcal{M} = 6$. The dynamical time is hereafter defined as $t_d \equiv L/(2\mathcal{M})$.

2.1. Uniform Grid Simulation at 1024^3

Our major production run is performed on a grid of 1024^3 points that allowed us to resolve a portion of the uncontaminated inertial range sufficient to get a first approximation for the low-order scaling exponents.

⁴ See <http://lca.ucsd.edu/>

We started the simulation at a lower resolution of 512^3 points and evolved the flow from the initial conditions for five dynamical times to stir up the gas in the box. Then we doubled the resolution and evolved the simulation for another $5t_d$ on a grid of 1024^3 points.

The time-average statistics were computed using 170 snapshots evenly spaced in time over the final segment of $4t_d$. (We allowed one dynamical time for flow relaxation at high resolution, so that it could reach a statistical steady state after regridding.) We used the full set of 170 snapshots to derive the density statistics, since the density field displays a very high degree of intermittency. This gave us a very large statistical sample, e.g. 2×10^{11} measurements were available to determine the probability density function (PDF) of the gas density discussed in Section 3.2. The time-average power spectra discussed in Sections 3.3, 3.5, 3.6, and 3.9 are also based on the full data set. The velocity structure functions presented in Section 3.4 are derived from a sample of 20% of the snapshots covering the same period of $4t_d$. The corresponding two-point PDFs of velocity differences were built on $2-4 \times 10^9$ pairs per snapshot each, depending on the pair separation.

2.2. AMR Simulations

The adaptive mesh refinement (AMR) simulation with effective resolution of 2048^3 points was initialized by evolving the flow on the root grid of 512^3 points for six dynamical times. Then one level of refinement by a factor of 4 was added that covers on average 50% of the domain volume. The grid is refined to better resolve strong shocks and to capture HD instabilities in the layers of strong shear. We use the native shock-detection algorithm of PPM, and we flag for refinement those zones that are associated with shocks with density jumps in excess of 2. We also track shear layers using the Frobenius norm $\|\partial_i u_j (1 - \delta_{ij})\|_F$, see also Kritsuk et al. (2006). This second refinement criterion adds about 20% more flagged zones that would be left unrefined if only the refinement on shocks were used. The simulation was continued with AMR for only $1.2t_d$, which allows enough time for relaxation of the flow at high resolution, but does not allow us to perform time-averaging over many statistically independent snapshots. Therefore, we use the data from AMR simulations mostly to compare the quality of instantaneous statistical quantities from simulations with adaptive and nonadaptive meshes.

2.3. Random Forcing

The initial velocity field is used, after an appropriate renormalization, as a steady random force (acceleration) to keep the total kinetic energy within the box on an approximately constant level during the simulations. The force we applied is isotropic in terms of the total specific kinetic energy per dimension, $\overline{u_{0,x}^2} = \overline{u_{0,y}^2} = \overline{u_{0,z}^2}$, but its solenoidal ($\nabla \cdot \mathbf{u}_{0,S} \equiv 0$) and dilatational ($\nabla \times \mathbf{u}_{0,D} \equiv 0$) components are anisotropic, since one of the three directions is dominated by the large-scale compressional modes, while the other two are mostly solenoidal. The distribution of the total specific kinetic energy

$$\mathcal{E} \equiv \frac{1}{2} \int_{\mathcal{V}} u^2 dV = \mathcal{E}_S + \mathcal{E}_D \quad (3)$$

between the solenoidal \mathcal{E}_S and dilatational \mathcal{E}_D components is such that $\chi_0 \equiv \mathcal{E}_{0,S}/\mathcal{E}_0 \approx 0.6$. The forcing field is helical, but the mean helicity is very low, $\overline{h_0^2} \ll \overline{h_0^2}$, where the helicity h

is defined as

$$h \equiv \mathbf{u} \cdot \nabla \times \mathbf{u}. \quad (4)$$

Note that in compressible flows with an isothermal equation of state the mean helicity is conserved, as in the incompressible case, since the Ertel's potential vorticity is identically zero (Gaffet 1985).

3. RESULTS

In this Section we start with a general quantitative description of our simulated turbulent flows and then derive their time-average statistical properties. We end up with assembling the pieces of this statistical picture in a context of a simple cascade model that extends the Kolmogorov phenomenology of incompressible turbulence into the compressible regime.

3.1. Time-evolution of Global Variables

The time variations of the rms Mach number and of the maximum gas density in the 1024^3 simulation are shown in Figs. 1 and 2. The kinetic energy oscillates between 18 and 22, roughly following the Mach number evolution. Note the highly intermittent bursts of activity in the plot of $\rho_{max}(t)$. The time-average enstrophy

$$\Omega \equiv \frac{1}{2} \int_{\mathcal{V}} |\boldsymbol{\omega}|^2 dV \approx 10^5 \quad (5)$$

and the Taylor scale

$$\lambda \equiv \sqrt{\frac{5E}{\Omega}} \approx 0.03 = 30\Delta, \quad (6)$$

where Δ is the linear grid spacing and $\boldsymbol{\omega} \equiv \nabla \times \mathbf{u}$ is the vorticity. The rms helicity grows by a factor of 7.7 in the initial phase of the simulation and then remains roughly constant at a level of 1.2×10^3 . While the conservation of the mean helicity is not built directly into the numerical method, it is still satisfied reasonably well. The value of $\overline{h}(t)$ is contained within $\pm 2\%$ of its rms value during the whole simulation.

If, instead of the Euler equations, we were to consider the Navier-Stokes equations with the explicit viscous terms, we could estimate the total viscous dissipation rate within the computational domain,

$$\epsilon \equiv \int_{\mathcal{V}} \Phi_i u_i dV, \quad (7)$$

where

$$\Phi_i \equiv \frac{2}{Re} \frac{\partial}{\partial x_j} \left(\mathfrak{S}_{ij} - \frac{1}{3} \nabla \cdot \mathbf{u} \delta_{ij} \right) \quad (8)$$

and

$$\mathfrak{S}_{ij} \equiv \frac{1}{2} \left(\frac{\partial u_i}{\partial x_j} + \frac{\partial u_j}{\partial x_i} \right) \quad (9)$$

is the symmetric rate-of-strain tensor, and the integration is done over the volume of the domain $\mathcal{V} = 1$. Using vector identities, Φ can be rewritten through the vorticity $\boldsymbol{\omega}$ and the dilatation $\nabla \cdot \mathbf{u}$ as

$$\Phi = -\frac{1}{Re} \left(\nabla \times \boldsymbol{\omega} - \frac{4}{3} \nabla \nabla \cdot \mathbf{u} \right), \quad (10)$$

and, by partial integration in equation (7),

$$\epsilon = -\frac{1}{Re} \left(\langle |\nabla \times \mathbf{u}|^2 \rangle + \frac{4}{3} \langle |\nabla \cdot \mathbf{u}|^2 \rangle \right), \quad (11)$$

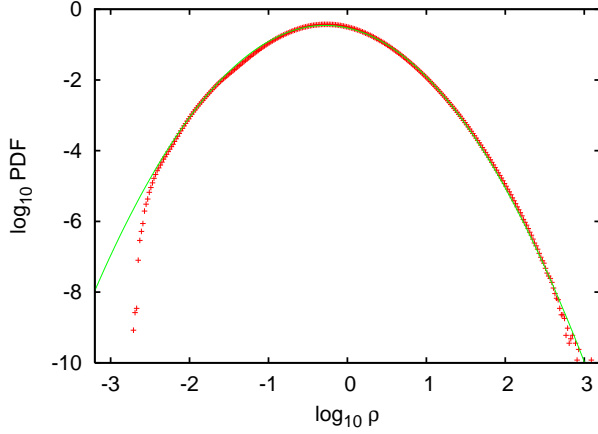


FIG. 3.— Probability density function for the gas density and the best-fit lognormal approximation. Note the excellent fit quality over eight decades in the probability along the high-density wing of the PDF. The sample size is 2×10^{11} .

where the two terms on the right-hand side of equation (11) describe the mean dissipation rate due to solenoidal and dilatational velocities, respectively, $\epsilon = \epsilon_S + \epsilon_D$.

In our Euler simulations, the role of viscous dissipation is played by the numerical diffusivity of PPM. This numerical dissipation does not necessarily have the same or similar functional form as the one used in the Navier-Stokes equations. It is still instructive, however, to get a flavor of the numerical dissipation rate by studying the properties of the vorticity and dilatation. The so-called small-scale compressive ratio (Kida & Orszag 1990, 1992),

$$r_{CS} \equiv \frac{\langle |\nabla \cdot \mathbf{u}|^2 \rangle}{\langle |\nabla \cdot \mathbf{u}|^2 \rangle + \langle |\nabla \times \mathbf{u}|^2 \rangle}, \quad (12)$$

represents the relative importance of the dilatational component at small scales. The time-average $\overline{r_{CS}} \approx 0.28$. The mean fraction of the dissipation rate that depends solely on the solenoidal velocity component, $\epsilon_S/\epsilon \approx 0.65$. Even though the two-dimensional shock fronts are dominating the geometry of the density distribution in the dissipation range (see Section 3.8), the dissipation rate itself is dominated by the solenoidal velocity component that tracks corrugated shocks due to vortex stretching in the associated strong shear flows.

3.2. Density PDF

In isothermal turbulence the gas density does not correlate with the local Mach number. As a result, the density PDF follows a lognormal distribution (Vazquez-Semadeni 1994; Padoan et al. 1997; Passot & Vázquez-Semadeni 1998; Nordlund & Padoan 1999; Biskamp 2003). Fig. 3 shows our results for the time-average density PDF and its best-fit lognormal representation

$$p(\ln \rho) d \ln \rho = \frac{1}{\sqrt{2\pi\sigma^2}} \times \exp \left[-\frac{1}{2} \left(\frac{\ln \rho - \overline{\ln \rho}}{\sigma} \right)^2 \right] d \ln \rho, \quad (13)$$

where the mean of the logarithm of the density, $\overline{\ln \rho}$, is determined by

$$\overline{\ln \rho} = -\sigma^2/2. \quad (14)$$

The lack of a Mach number–density correlation is illustrated in Fig. 4 where we show the two-dimensional PDF for the density and Mach number. The density distribution is very broad due to the very high degree of compressibility under

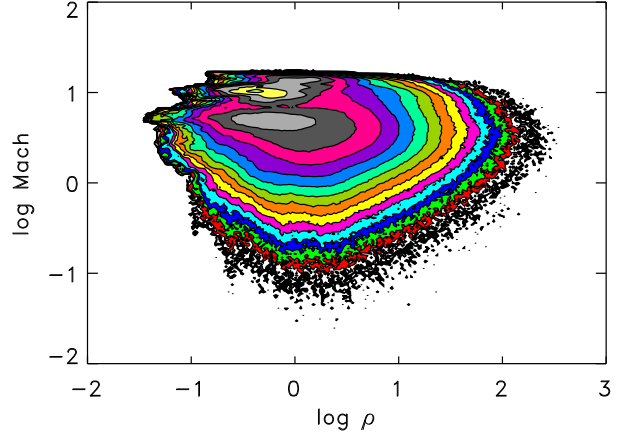


FIG. 4.— Two-dimensional probability density function for the gas density and Mach number. The data here are based on a subvolume of $700 \times 500 \times 250 \approx 10^8$ points from a representative snapshot at $t = 7 t_d$ that we will also use later in Figs. 14 and 17. The contours show the probability density levels separated by factors of 2.

isothermal supersonic conditions. The density contrast $\sim 10^6$ is orders of magnitude higher than in the transonic case at $\gamma = 1.4$ studied by Porter et al. (2002). Note the excellent quality of the lognormal fit in Fig. 3, particularly at high densities, over more than eight decades in the probability and a very low noise level in the data.

If we express the standard deviation σ as a function of Mach number \mathcal{M} as

$$\sigma^2 = \ln(1 + b^2 \mathcal{M}^2), \quad (15)$$

we get the best-fit value of $b \approx 0.260 \pm 0.001$ for $\log_{10} \rho \in [-2, 2]$, which is smaller than the $b \approx 0.5$ determined in Padoan et al. (1997) for supersonic MHD turbulence. The powerful intermittent bursts in $\rho_{max}(t)$ (see Fig. 3) correspond to large departures from the time-average PDF caused by head-on collisions of strong shocks. These events are usually followed by strong rarefactions that are seen as large oscillations in the low-density wing of the PDF and also in the density power spectrum. Intermittency is apparently very strong in supersonic turbulence.

3.3. Velocity Power Spectra, Bottleneck Phenomenon, Numerical Dissipation, and Convergence

We define the velocity power spectrum $\mathcal{E}(\mathbf{k})$ (or the *specific kinetic energy spectral density*) in terms of the Fourier transform of the velocity \mathbf{u}

$$\tilde{\mathbf{u}}(\mathbf{k}) = \frac{1}{(2\pi)^3} \int_{\mathcal{V}} \mathbf{u}(\mathbf{x}) e^{-2\pi i \mathbf{k} \cdot \mathbf{x}} d\mathbf{x} \quad (16)$$

as the square of the Fourier coefficient

$$\mathcal{E}(\mathbf{k}) \equiv \frac{1}{2} |\tilde{\mathbf{u}}(\mathbf{k})|^2, \quad (17)$$

and then we define the three-dimensional velocity power spectrum as

$$\mathcal{E}(k) \equiv \int_{\mathcal{V}} \mathcal{E}(\mathbf{k}) \delta(|\mathbf{k}| - k) d\mathbf{k}, \quad (18)$$

where $\delta(k)$ is the Dirac δ -function. The integration of the velocity power spectrum gives the specific kinetic energy (cf. eq. [3]),

$$\mathcal{E} \equiv \int \mathcal{E}(k) dk = \frac{1}{2} \langle \mathbf{u}^2 \rangle. \quad (19)$$

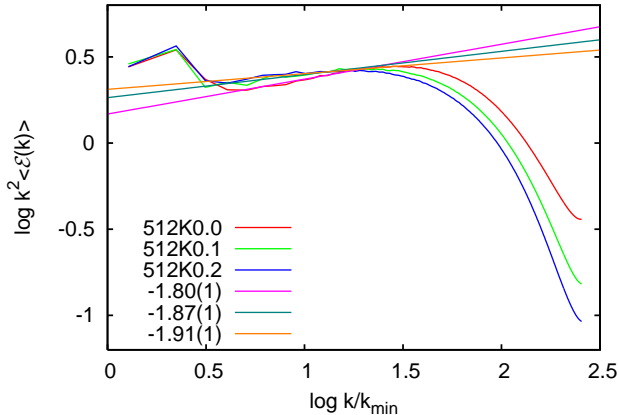


FIG. 5.— Time-averaged velocity power spectra as a function of PPM diffusion coefficient $K = 0.0, 0.1,$ and 0.2 at resolution of 512^3 grid points. The straight lines show the best linear fits to the spectra obtained for $\log k/k_{min} \in [0.6, 1.3]$. The inertial range is barely resolved, since the driving scale overlaps with the bottleneck-contaminated interval. The slope of the “flat” part of the spectrum is mainly controlled by numerical diffusion.

Our main focus in this Section is on the self-similar scaling of the power spectrum in the inertial range

$$\mathcal{E}(k) \sim k^{-\beta} \quad (20)$$

that is limited by the kinetic energy input from the random force on large scales ($k/k_{min} < 2$) and by the spectrum flattening in the near-dissipation part of the inertial range due to the so-called bottleneck effect related to a three-dimensional non-local mechanism of energy transfer between modes of differing length scales (Falkovich 1994).

The bottleneck phenomenon has been observed both experimentally and in numerical simulations (e.g., Porter et al. 1994; Kaneda et al. 2003; Dobler et al. 2003; Haugen & Brandenburg 2004). The strength of the bottleneck depends on the way the dissipation scales with the wavenumber, and the effect is more pronounced when the dissipation grows faster than $\sim k^2$ (Falkovich 1994). When we numerically integrate the Euler equations using PPM, the dissipation is solely determined by the method and affects scales smaller than 32Δ (Porter & Woodward 1994). According to Porter et al. (1992a), the effective numerical viscosity of PPM has a wavenumber dependency intermediate between $\sim k^4$ and $\sim k^5$. The high-order basic reconstruction scheme of PPM is designed to improve resolution in shocks and contact discontinuities and, therefore, numerical diffusion is controlled by various switches and is nonuniform in space.

An addition of small diffusive flux near shocks⁵ changes the scaling properties of numerical dissipation and reduces the flattening of the spectrum due to the bottleneck phenomenon. When the grid is not large enough to resolve the basic flow, the bottleneck bump in the spectrum is smeared and can be easily misinterpreted as a shallower spectrum. Figure 5 shows how the slope of the “flat” section in the velocity power spectrum at 512^3 depends on the value of the diffusion coefficient K . The inertial range is unresolved in all three cases shown. The measured slope $\beta(K)$ changes from 1.91 ± 0.01 to 1.80 ± 0.01 as the diffusion coefficient decreases from 0.2 to zero and the bottleneck bump gets stronger. While the statistical uncertainty of estimated power indices based on the

⁵ This is controlled by the parameter K in equation (4.5) in Colella & Woodward (1984).

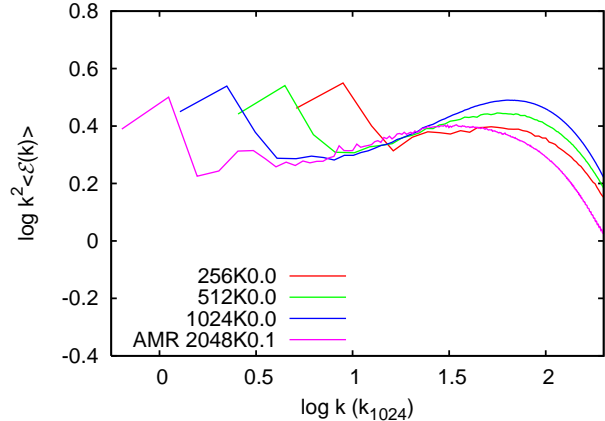


FIG. 6.— Compensated velocity power spectra from uniform grid PPM simulations at resolutions $256^3, 512^3, 1024^3,$ and from AMR simulation with effective resolution of 2048^3 grid points. The wavenumbers are normalized to match k/k_{min} of the 1024^3 simulations at the Nyquist frequency. The diffusion coefficient $K = 0$ for the uniform grid simulations, and $K = 0.1$ for the AMR simulation. All power spectra are time-averaged over $t \in [6, 10] t_d$ with the exception of the AMR one that is taken at $t = 7.2 t_d$. The spectra demonstrate convergence for the inertial range of scales.

fitting procedure is rather small, the variation of β as a function of the diffusion coefficient is substantial and accounts for $\sim 33\%$ of the difference between Burgers and Kolmogorov slopes! Clearly, it is difficult to get reliable estimates for the inertial range power indices from simulations with resolution up to 512^3 , since the slope of the spectrum is so dependent on numerical diffusivity. To study higher Mach number flows with PPM, an even higher resolution would be required. Note that with other numerical methods, one typically needs to use even larger grids, since the amount of dissipation provided by PPM is quite small compared to what is usually given in finite-difference schemes. In low-resolution simulations with high numerical dissipation that depends on the wavenumber as $\sim k^2$ or weaker, the power spectra appear steeper than they would have been when properly resolved.

In simulations with AMR, the grid resolution is nonuniform, and scaledependence (as well as nonuniformity) of numerical diffusion becomes even more complex. One should generally expect a more extended range of wavenumbers affected by numerical dissipation in AMR simulations than in uniform grid simulations, when the effective resolution is the same. The dependence of the effective numerical diffusivity on the wavenumber in the AMR runs is, therefore, weaker than in simulations on uniform grids, and the bottleneck bump should be suppressed.

In Figure 6 we combined the velocity power spectra from the unigrid simulations at $256^3, 512^3,$ and 1024^3 grid points with the diffusion coefficient $K = 0$ to illustrate the convergence of the inertial range scaling with the improved resolution. All three simulations were performed with the same large-scale driving force, and the spectra were averaged over the same time interval, so the only difference between them is the resolution-controlled effective Reynolds number. We plotted the compensated spectra $k^2 \mathcal{E}(k)$ to specifically exaggerate the relatively small changes in the slopes. The over-plotted power spectrum from a single snapshot from our largest to date AMR simulation with the effective resolution of 2048^3 grid points seems to confirm the (self-) convergence. Thus, one may hope that our estimates of the scaling exponents based on the time-averaged statistics from the 1024^3 simulation will not be too far off from those that correspond to

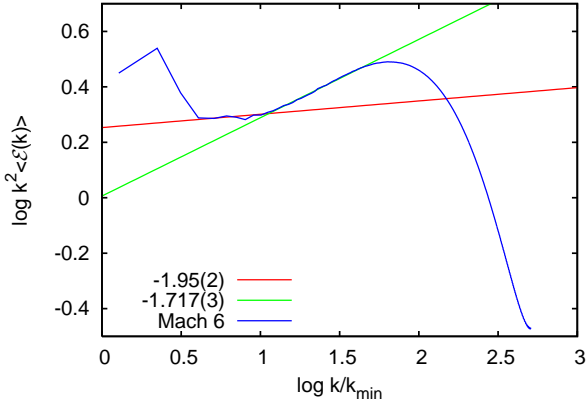


FIG. 7.— Velocity power spectrum compensated by k^2 . Note a large-scale excess of power at $\ell \in [256, 1024]\Delta$ due to external forcing, a short straight section in the uncontaminated inertial subrange $\ell \in [40, 256]\Delta$, and a small-scale excess at $\ell < 40\Delta$ due to the bottleneck phenomenon. The straight lines represent the least-squares fits to the data for $\log k/k_{\min} \in [0.6, 1.1]$ and $\log k/k_{\min} \in [1.2, 1.7]$.

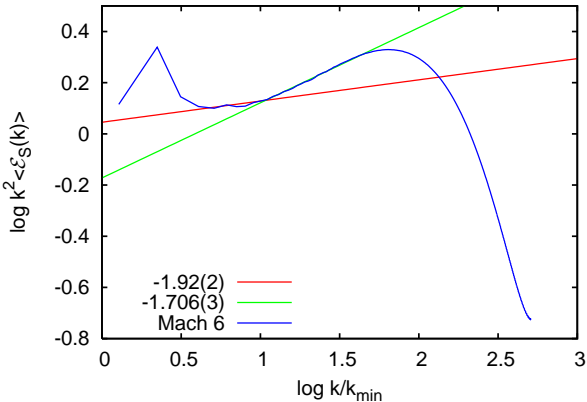


FIG. 8.— Same as Fig. 7, but for the solenoidal velocity component.

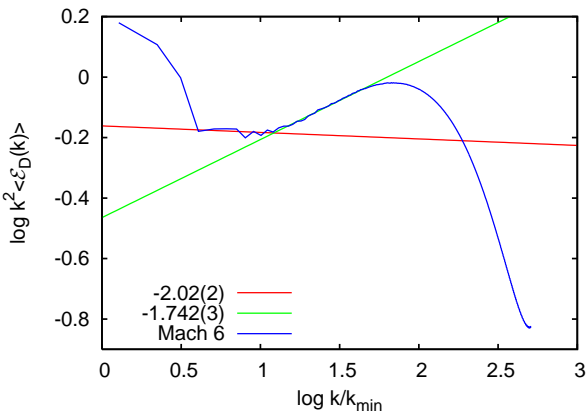


FIG. 9.— Same as Fig. 7, but for the dilatational velocity component.

$\text{Re} \rightarrow \infty$. We further validate this statement in Section 3.4, where we discuss the scaling properties of the velocity structure functions. Note also the suppression of the bottleneck bump visible in the AMR spectrum that occurs due to the higher effective diffusivity as we discussed earlier.

Our reference velocity power spectrum from the 1024^3 sim-

ulation is repeated in Fig. 7 with the best-fit linear approximations. It follows a power law with an index $\beta = 1.95 \pm 0.02$ within the range of scales $\ell \in [40, 256]\Delta$ and has a shallower slope, $\beta_b = 1.72$, for the bottleneck bump. After Helmholtz decomposition, $\mathcal{E}(k) = \mathcal{E}_S(k) + \mathcal{E}_D(k)$, the spectra for the solenoidal and dilatational components show the inertial range power indices of $\beta_S = 1.92 \pm 0.02$ and $\beta_D = 2.02 \pm 0.02$, respectively, see Figs. 8 and 9. The difference in the slopes of $\mathcal{E}_S(k)$ and $\mathcal{E}_D(k)$ is about 5σ , i.e. significant. Both spectra display flattening due to the bottleneck with indices of $\beta_{b,S} = 1.70$ and $\beta_{b,D} = 1.74$ in the near-dissipative range. The fraction of energy in dilatational modes quickly drops from about 50% at $k = k_{\min}$ down to 30% at $k/k_{\min} \approx 50$ and then returns back to a level of 45% at the Nyquist frequency.

In summary, the inertial range scaling of the velocity power spectrum in highly compressible turbulence tends to be closer to the Burgers scaling with a power index of $\beta = 2$ rather than to the Kolmogorov $\beta = 5/3$ scaling suggested for the mildly compressible transonic simulations by Porter et al. (2002). The inertial range scaling exponents of the power spectra for the solenoidal and dilatational velocities are not the same, with the latter demonstrating a steeper Burgers scaling, containing about 30% of the total specific kinetic energy, and being responsible for up to 35% of the global dissipation rate (see Section 3.1).

3.4. Velocity Structure Functions

To substantiate this result, we studied the scaling properties of the velocity structure functions (e.g., Monin & Yaglom 1975)

$$S_p(\ell) \equiv \langle |\mathbf{u}(\mathbf{r} + \boldsymbol{\ell}) - \mathbf{u}(\mathbf{r})|^p \rangle \quad (21)$$

of orders $p = 1, 2$, and 3 , where the averaging $\langle \dots \rangle$ is taken over all positions \mathbf{r} and all orientations of $\boldsymbol{\ell}$ within the computational domain. Both longitudinal ($\mathbf{u} \parallel \boldsymbol{\ell}$) and transverse ($\mathbf{u} \perp \boldsymbol{\ell}$) structure functions can be well approximated by power laws in the inertial range

$$S_p(\ell) \propto \ell^{\zeta_p}, \quad (22)$$

see Figures 10-12. The low-order structure functions are less susceptible to the bottleneck contamination and might be better suited for deriving the scaling exponents (Dobler et al. 2003).⁶ Let us now check how close the exponents derived from the data are to the K41 prediction $\zeta_p = p/3$.

It is natural to begin with the second-order structure functions, since the velocity power spectrum $\mathcal{E}(k)$ is the Fourier transform of $S_2(\ell)$ and therefore $\beta = \zeta_2 + 1$. The best-fit second-order exponents measured for the range of scales ℓ between 32Δ and 256Δ , $\zeta_2^{\parallel} = 0.952 \pm 0.004$ and $\zeta_2^{\perp} = 0.977 \pm 0.008$, are substantially larger than the K41 value of $2/3$ and, within the statistical uncertainty, agree with our measured velocity power index $\beta = 1.95 \pm 0.02$. In homogeneous isotropic incompressible turbulence, S_2^{\perp} is uniquely determined by S_2^{\parallel} (and vice versa) via the first de Kármán & Howarth (1938) relation,

$$S_2^{\perp} = S_2^{\parallel} + \frac{\ell}{2} S_2^{\parallel \prime}. \quad (23)$$

For the K41 inertial range velocity scaling, this translates into

$$S_2^{\perp} = \frac{4}{3} S_2^{\parallel}. \quad (24)$$

⁶ Note, however, that the bottleneck corrections grow with the order p (Falkovich 1994) and influence the structure functions in a nonlocal fashion, mixing small- and large-scale information (Dobler et al. 2003; Davidson & Pearson 2005).

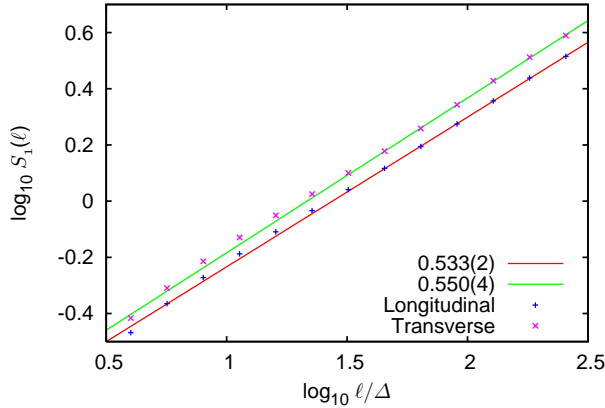


FIG. 10.— First-order velocity structure functions and the best-fit power laws for $\log_{10}(\ell/\Delta) \in [1.5, 2.5]$.

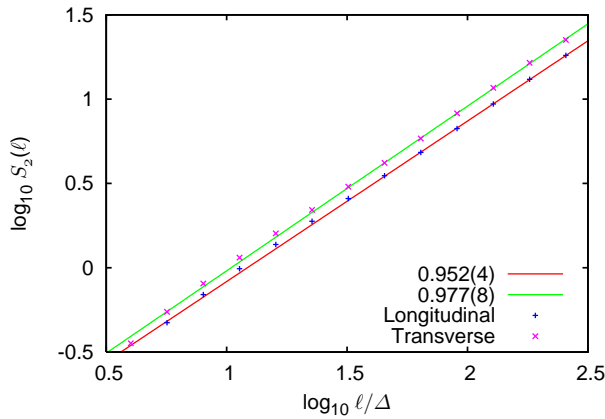


FIG. 11.— Same as Fig. 10, but for the second-order structure functions.

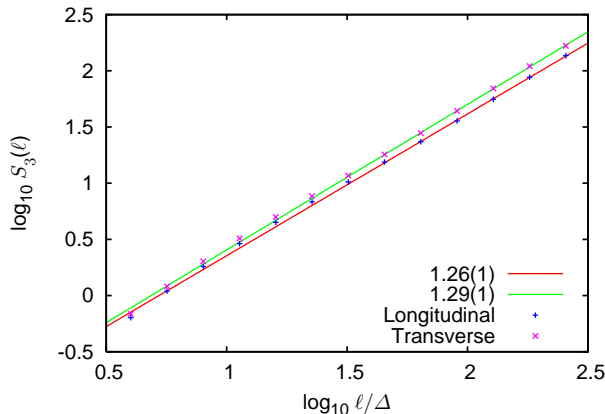


FIG. 12.— Same as Fig. 10, but for the third-order structure functions.

At Mach 6, the 2nd-order longitudinal and transverse structure functions are also approximately parallel to each other in the $(\log S, \log \ell)$ -plane, but the offset between them, $S_2^\perp/S_2^\parallel \approx 1.27$, is somewhat smaller than the K41 value of $4/3$. This suggests that in highly compressible regimes some generalization of the first Kármán-Howarth relation still remains valid, even though a substantial fraction of the specific kinetic energy (up to $1/3$ at $\mathcal{M} = 6$) is concentrated in the dilatational component (cf. Moyal 1951; Samtaney et al. 2001).

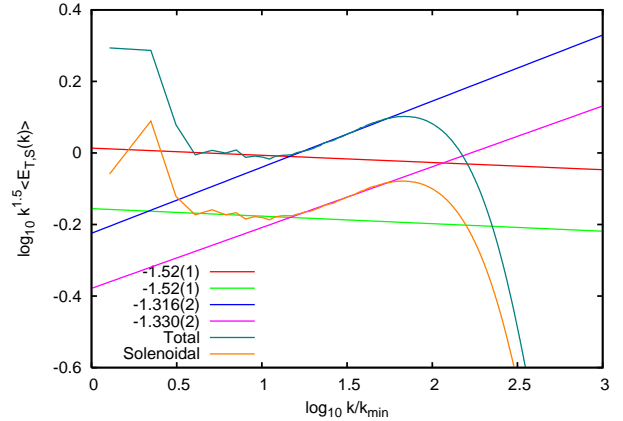


FIG. 13.— Time-average total kinetic energy spectrum $E(k)$ and solenoidal kinetic energy spectrum $E_S(k)$, both compensated by $k^{3/2}$. The straight lines represent the least-squares fits to the data for $\log k/k_{\min} \in [0.5, 1.2]$ and $\log k/k_{\min} \in [1.2, 1.8]$. The inertial range slopes of the total and the solenoidal kinetic energy spectrum are the same within the statistical errors, which is not the case for the velocity power spectra. The dilatational component (not shown) also has the same slope.

The first-order exponents $\zeta_1^\parallel = 0.533 \pm 0.002$ and $\zeta_1^\perp = 0.550 \pm 0.004$ are again significantly larger than the K41 index of $1/3$ but also considerably smaller than the index of 1 for the Burgers model (e.g., Frisch & Bec 2001). Observationally determined exponents for the molecular cloud turbulence are normally found within the range from 0.4 to 0.8 (Brunt et al. 2003), in reasonable agreement with our result.

We find that the third-order scaling exponents $\zeta_3^\parallel = 1.26 \pm 0.01$ and $\zeta_3^\perp = 1.29 \pm 0.01$ are also noticeably off from $\zeta_3 = 1$ predicted by K41 in the incompressible limit. Our measurements for the three low-order exponents roughly agree with the estimates $\zeta_1^\perp \approx 0.5$, $\zeta_2^\perp \approx 0.9$, and $\zeta_3^\perp \approx 1.3$ obtained by Boldyrev et al. (2002) from numerical simulations of isothermal Mach 10 MHD turbulence at a resolution of 500^3 points. A rigorous result $\zeta_3 = 1$ holds for incompressible Navier-Stokes turbulence (Kolmogorov 1941c, “4/5” law) and for incompressible MHD (Politano, & Pouquet 1998). Strictly speaking, $\zeta_3 = 1$ is proved only for the longitudinal structure function, S_3^\parallel , (Kolmogorov 1941c) and for certain mixed structure functions (Politano, & Pouquet 1998), and in both cases the absolute value of the velocity difference is *not* taken (cf. eq. [21]), but still we know from numerical simulations that $\zeta_3 \approx 1$ in a compressible transonic regime for the absolute velocity differences, as in equation (21) (Porter et al. 2002).

The fact that in supersonic turbulence $\zeta_3 \neq 1$ should be accounted for in extensions of incompressible turbulence models into the strongly compressible regime. One approach is to consider relative (to the third order) scaling exponents as more universal (Dubrulle 1994) and reformulate the models in terms of the relative exponents (cf. Boldyrev 2002; Boldyrev et al. 2002). In many low-resolution simulations, exploiting the so-called extended self-similarity hypothesis (Benzi, et al. 1993, 1996), the foundations of which are not yet fully understood (see, e.g., Sreenivasan & Bershadskii 2005), is the only resort to at least measure the relative exponents. Another approach is to consider statistics of mixed quantities, like $\rho^\eta \mathbf{u}$, in place of pure velocity statistics naively inherited from incompressible regime studies. We shall discuss the options for the former approach below and then return to the latter in Sections 3.5 and 3.9.

The *relative* scaling exponents $Z_p \equiv \zeta_p/\zeta_3$ of the first and the second order we obtain from our simulations are still somewhat higher than their incompressible nonintermittent analogues $1/3$ and $2/3$; $Z_1^\parallel = 0.42$, $Z_1^\perp = 0.43$, and $Z_2^\parallel \approx Z_2^\perp = 0.76$. This situation is similar to a small discrepancy between the K41 predictions and experimental measurements that stimulated Obukhov (1962) and Kolmogorov (1962) to supplement the K41 theory by “intermittency corrections.” If we follow a similar path in our strongly compressible case and estimate the “corrected” exponents using the Boldyrev et al. (2002) formula, which is similar to the She & Leveque (1994) model, but assumes that the most singular dissipative structures are not one-dimensional vortex filaments but rather two-dimensional shock fronts,

$$Z_p = \frac{p}{9} + 1 - \left(\frac{1}{3}\right)^{p/3}, \quad (25)$$

we get the exponents $Z_1 = 0.42$ and $Z_2 = 0.74$ that are very close to our estimates. One can argue though that at high Mach numbers, the dilatational velocities constitute a substantial part of the total specific kinetic energy, and therefore, a double set of singular velocity structures and their associated dynamics would lead to a compound Poisson statistic instead of a single Poisson process incorporated in equation (25) (see She & Waymire 1995). To check whether this is indeed true or not, one needs to collect information about higher order statistics from simulations at resolution better than 1024^3 .

3.5. Kinetic Energy Spectrum

To explore the second option outlined in Section 3.4, we considered the energy-spectrum function $E(k)$ built on $\mathbf{w} \equiv \sqrt{\rho} \mathbf{u}$ (e.g., Lele 1994) in addition to $\mathcal{E}(k)$ that depends solely on the velocity \mathbf{u} and is traditionally used for characterizing incompressible turbulence. We defined the kinetic energy spectral density $E(\mathbf{k})$ as the square of the Fourier coefficient

$$E(\mathbf{k}) \equiv \frac{1}{2} |\tilde{\mathbf{w}}(\mathbf{k})|^2 \quad (26)$$

determined by the Fourier transform

$$\tilde{\mathbf{w}}(\mathbf{k}) = \frac{1}{(2\pi)^3} \int_{\mathcal{V}} \mathbf{w}(\mathbf{x}) e^{-2\pi i \mathbf{k} \cdot \mathbf{x}} d\mathbf{x}. \quad (27)$$

Then we used the standard definition of the three-dimensional kinetic energy spectrum function

$$E(k) \equiv \int_{\mathcal{V}} E(\mathbf{k}) \delta(|\mathbf{k}| - k) d\mathbf{k}, \quad (28)$$

where $\delta(k)$ as before is the δ -function. To avoid a possible terminological confusion, in the following we always refer to $\mathcal{E}(k)$ as the velocity power spectrum and to $E(k)$ as the kinetic energy spectrum

$$E \equiv \int E(k) dk = \frac{1}{2} \langle \rho \mathbf{u}^2 \rangle. \quad (29)$$

At low Mach numbers, the scaling exponents of $E(k)$ and $\mathcal{E}(k)$ are nearly the same. However, while $\mathcal{E}(k)$ does not change much as the Mach number approaches unity (e.g., Porter et al. 2002), the slope of $E(k)$ gets shallower already by $\mathcal{M} = 0.9$ (Kida & Orszag 1992, based on simulations with 64^3 collocation points). Since at low Mach numbers the spectra are dominated by the solenoidal components, and the solenoidal velocity power spectrum hardly depends on the

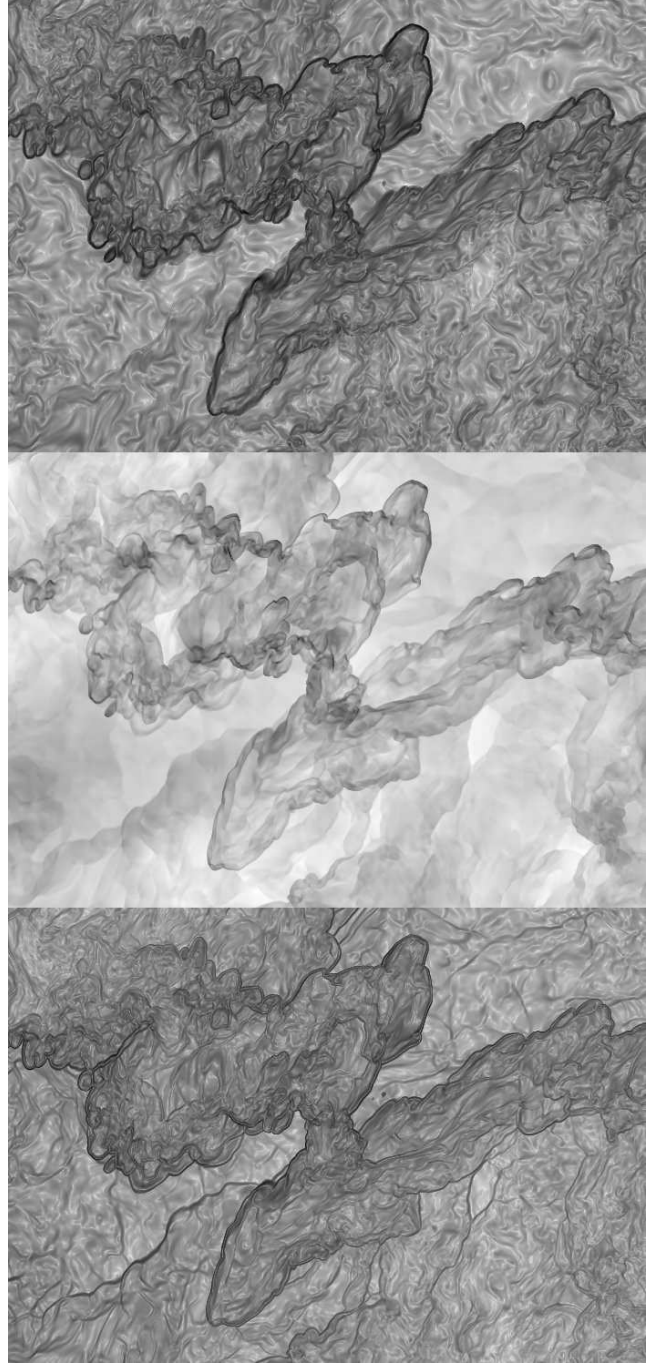


FIG. 14.— Enstrophy ($|\nabla \times \mathbf{u}|^2$; top), density (middle), and “denstrophy” ($|\nabla \times (\sqrt{\rho} \mathbf{u})|^2/\rho$; bottom) distributions in a slice through the center of the subvolume of the computational domain at $t = 7t_d$. The logarithmic gray-scale ramp is used to show the highest values in black and the lowest values in white.

Mach number, the departure of the slope of $E(k)$ from the slope of $\mathcal{E}(k)$ is mostly due to the sensitivity of the solenoidal part of the kinetic energy spectrum to the density–vorticity correlation that is felt already around $\mathcal{M} \sim 0.5$. Shallow slopes for $E(k)$ with power indices around $-3/2$ were also detected in MHD simulations of highly supersonic super-Alfvénic turbulence (Li et al. 2004, 512^3 grid points).

In the inertial range, the time-averaged kinetic energy spectrum scales as $E(k) \sim k^{-\beta}$ with $\beta = 1.52 \pm 0.01$ (see Fig. 13). The spectrum displays flattening at high wavenumbers due to the bottleneck effect, which is similar to what we have already

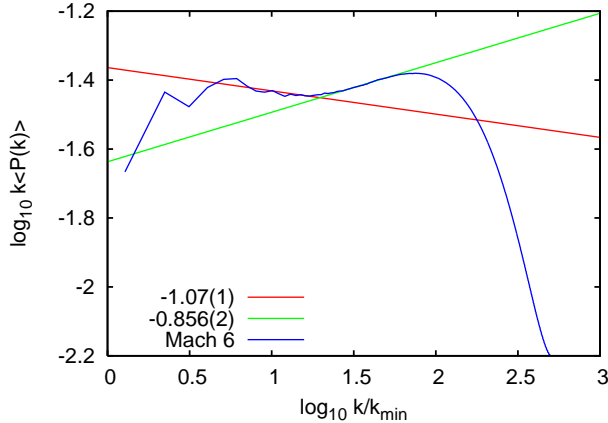


FIG. 15.— Time-average density power spectrum compensated by k . The straight lines represent the least-squares fits to the data for $\log k/k_{\min} \in [0.6, 1.3]$ and $\log k/k_{\min} \in [1.4, 1.7]$.

seen in the velocity power spectra $\mathcal{E}(k)$. The flat part scales roughly as $\sim k^{-1.3}$ and occupies the same range of wavenumbers as in the velocity spectrum. Since the kinetic energy spectrum is sensitive to the rather sporadic activity of density fluctuations, time-averaging is essential to get a robust estimate for the power index.

We performed a decomposition of $\mathbf{w} \equiv \sqrt{\rho}\mathbf{u}$ into the solenoidal and dilatational parts $\mathbf{w}_{S,D}$ such that $\nabla \cdot \mathbf{w}_S = \nabla \times \mathbf{w}_D \equiv 0$, and computed the energy spectra for both components, $E(k) = E_S(k) + E_D(k)$. The inertial range spectral exponents for the solenoidal and dilatational components are the same, $\beta = 1.52 \pm 0.01$ for both, and also coincide with the slope of $E(k)$. This remarkable property of $E(k)$ suggests that in the supersonic regime⁷ we are dealing with a single compressible cascade of kinetic energy where the density fluctuations provide a tight coupling between the solenoidal and dilatational modes of \mathbf{w} . This picture is similar in spirit to that discussed by Kornreich & Scalo (2000, in their Section 3.7). However, in contrast to Kornreich & Scalo (2000), our simulations demonstrate that nonlinear HD instabilities are heavily involved in the kinetic energy transfer through the hierarchy of scales. The association of \mathbf{w} with the kinetic energy distribution as a function of scale makes this quantity a better candidate than the pure velocity \mathbf{u} for employing in compressible cascade models, since \mathbf{w} uniquely represents the physics of the cascade and there is no need to track the variation of $\mathcal{E}_D(k)/\mathcal{E}(k)$ as a function of wavenumber in the inertial subrange in addition to variations with the rms Mach number.

The total kinetic energy power is dominated by the solenoidal component \mathbf{w}_S over the whole spectrum. Within the inertial range, $E_S(k)$ contributes about 68% of the total power, then $\sim 66\%$ in the bottleneck-contaminated interval, and up to $\sim 74\%$ further down at the Nyquist frequency. Compare with the solenoidal part of the velocity power, $\mathcal{E}_S(k)$, that constitutes about 65%–70% within the inertial range and only 55% of the total power at the Nyquist frequency (see Section

⁷ In our Mach 6 simulations at 1024^3 , the sonic scale ℓ_s such that $u(\ell_s) \sim c = 1$ is located in the middle of the bottleneck bump, and thus, the velocities within the inertial range are supersonic. One could possibly detect a break in the velocity power spectrum from a steep Burgers-like supersonic scaling at low k to a shallow Kolmogorov-like transonic scaling at higher wavenumbers in Mach 6 simulations with resolution of 4000^3 grid points or higher. Note, that as we show later in Section 3.9, the power spectrum of $\rho^{1/3}\mathbf{u}$ would not show such a break and would instead approximately follow the Kolmogorov 5/3 law all over the inertial interval.

3.3).

Figure 14 illustrates the difference in structures seen in the enstrophy field (*top*) and in the “denstrophy” field ($|\nabla \times (\sqrt{\rho}\mathbf{u})|^2/\rho$, *bottom*) that helps to understand the small-scale excess of power in $E_S(k)$ with respect to $\mathcal{E}_S(k)$. While the corrugated shock surfaces (U-shapes), which are also the regions of very strong shear, are seen as dark wormlike structures of excess enstrophy and denstrophy in both the top and the bottom panels of Fig. 14, nearly planar shock fronts that carry a negligible amount of shear (this is also why they remain planar) are clearly missing in the enstrophy plot. Since the denstrophy field contains a greater number of sharper small-scale structures, it should be expected that $E_S(k)$ carries more small-scale power than $\mathcal{E}_S(k)$. Overall, the structures captured as intense by the denstrophy field closely follow the regions of high energy dissipation rate (see the integrand in eq. [7] and Fig. 17, *bottom left*).

3.6. Density Power Spectrum

The power spectrum of the gas density shows a short straight section with a slope of -1.07 ± 0.01 in the range of scales from 250Δ down to 40Δ followed by flattening due to a power pileup at higher wavenumbers, see Fig. 15. Similar power-law sections, and excess of power in the same wavenumber ranges were seen earlier in the velocity and the kinetic energy power spectra, Figs. 7 and 13.

At the resolution of 512^3 , the bottleneck bump at high wavenumbers and the external forcing at low k leave essentially no room for the uncontaminated inertial range in k -space, even though the density spectrum at 512^3 (not shown) also has a straight power-law section. At 512^3 , the slope of the density power spectrum, -0.90 ± 0.02 , is substantially shallower than -1.07 at 1024^3 . Thus, spectral index estimates based on low-resolution simulations bear large uncertainties due to the bottleneck contamination. We also note that the time-averaging over many snapshots is essential to get the correct slope for the density power spectrum, since the density exhibits strong variations on very short (compared to t_d) time-scales. The spectrum tends to get shallower after collisions of strong shocks, when the PDF’s high-density wing rises above its average lognormal representation.

There are good reasons to believe that in weakly compressible isothermal flows the three-dimensional density power spectrum scales in the inertial subrange as $\sim k^{-7/3}$ (Bayly et al. 1992). Our 512^3 transonic simulation at $\mathcal{M} = 1$ with purely solenoidal driving (not shown) returned a time-average power index of -1.6 ± 0.1 , which is probably still too shallow due to the unresolved inertial range (see also Section 3.3). An index of -1.7 at $\mathcal{M} = 1.2$ was obtained by Kim & Ryu (2005) at the same resolution (but with a more diffusive solver). Our simulations at higher resolution for $\mathcal{M} = 6$ give a slope of approximately -1.1 . At even higher Mach numbers, the spectra tend to flatten further. From the continuity arguments, there should exist a Mach number value \mathcal{M}_{41} such that the power index of the density spectrum is exactly $-5/3$, i.e. coincides with the Kolmogorov velocity spectrum power index. Since apparently $\mathcal{M}_{41} \lesssim 1$, subsonic (but not too subsonic) compressible turbulent flows should have near-Kolmogorov scaling, even for the density power spectrum (cf. Armstrong et al. 1995).

3.7. Coherent Structures in Supersonic Turbulence

Let us now look more carefully at the morphology of those structures in supersonic turbulence that determine its scaling

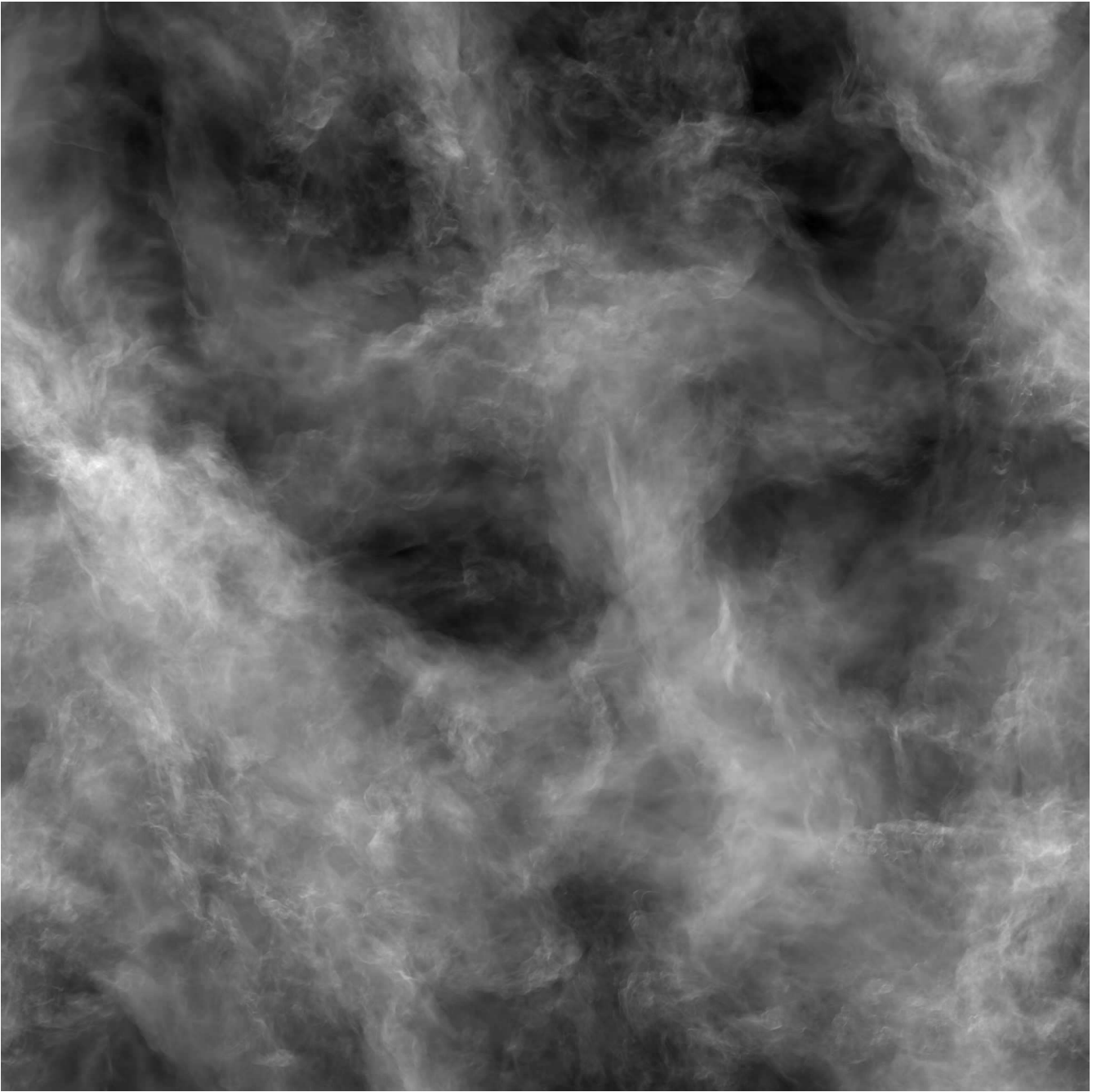


FIG. 16.— Logarithm of the projected density from a snapshot of the AMR simulation with effective grid resolution of 2048^3 zones. The standard linear gray-scale ramp shows the highest density peaks in white and the most underdense voids in black.

properties. The very first look at the projected density field shown in Figure 16 reveals a plethora of filamentary structures very similar to what one usually sees as cirrus clouds in the sky. This is roughly what one can directly observe, albeit with a somewhat poorer resolution, in the intensity maps of nearby molecular clouds and in the WC-type turbulent stellar winds from the Wolf-Rayet stars.

If one zooms in on a subvolume and takes a slab that is 5 times thinner than the whole domain, one will start seeing the elements of that cloudy structure, namely, numerous nested U- and V-shaped bow shocks or “Mach cones” (Kritsuk et al. 2006). Figure 17 shows an example of coherent structures that form in supersonic flows as a result of development and saturation of linear and nonlinear insta-

bilities in shear layers formed by shock interactions.⁸ The instabilities assist in breaking the dense post-shock gas layers into supersonically moving fragments. Due to their extremely high density contrast with the surrounding medium, the fragments behave as effectively solid obstacles with respect to the medium. These coherent structures are transient and form in supersonic collisions of counter-propagating flow patches or “blobs” (Kritsuk & Norman 2004; Heitsch et al. 2005; Kritsuk et al. 2006). Then they dissipate and similar structures appear again and again at other locations. The

⁸ The (incomplete) list of potential candidates includes the Kelvin-Helmholtz instability (Helmholtz 1868), the nonlinear supersonic vortex sheet instability (Miles 1957), and the nonlinear thin shell instability (Vishniac 1994).

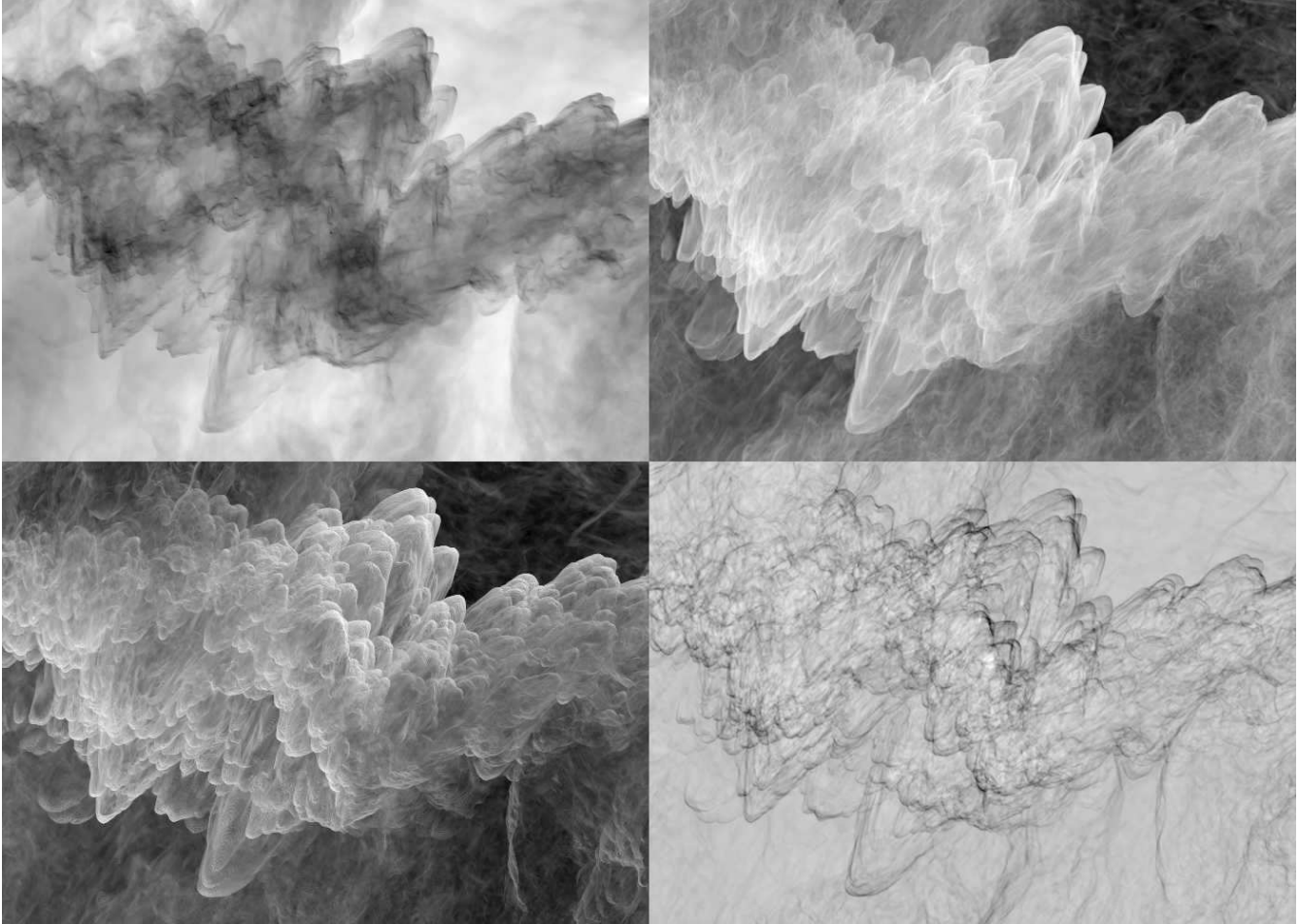


FIG. 17.— Coherent structures in Mach 6 turbulence at resolution of 1024^3 . Projections along the minor axis of a subvolume of $700 \times 500 \times 250$ zones for the density (*top left*), the enstrophy ($|\nabla \times \mathbf{u}|^2$; *top right*), the dissipation rate (the integrand $|\Phi \cdot \mathbf{u}|$ in eq. 7; *bottom left*), and the dilatation ($\nabla \cdot \mathbf{u}$; *bottom right*). The logarithmic gray-scale ramp shows the lower values as dark in all cases except for the density. The inertial subrange structures correspond to scales between 40 and 250 zones and represent a fractal with $D_m \approx 2.4$. The most singular structures in the dissipation range ($\ell < 30\Delta$) are shocks with fractal dimension $D_m = 2$.

nested V-shapes can be best seen in slabs with a finite thickness of the order of their characteristic size (i.e. $\sim 200\Delta$ in our 1024^3 run) that belongs to the resolved inertial subrange of scales. They are less noticeable in full-box projections where multiple structures of the same sort tend to overlap along the line of sight as in Figure 16. Since the “cones” are essentially three-dimensional, they can also be hardly seen in thin slices, see Fig. 14. Patterns of the same morphology were identified in the peripheral parts of the M1-67 nebula observed in H_α emission by the *Hubble Space Telescope* (Grosdidier et al. 2001).

3.8. Fractal Dimension of the Mass Distribution

It is known from observations and experiments that the distribution of dissipation in turbulent flows is intrinsically intermittent and this intermittency bears a hierarchical nature. This fact is in apparent contradiction with the K41 theory that assumes that the rate of dissipation is uniform in space and constant in time. Mandelbrot (1974) introduced a new concept of the “intrinsic fractional dimension of the carrier,” D , that characterizes the geometric properties of a subset of the whole volume of turbulent flow where the bulk of intermittent dissipation occurs. He also studied the relation between D and scaling properties of turbulence. In particular, he suggested that isosurfaces of scalars (such as concentration or temperature) in turbulent flows with Burgers and Kolmogorov statis-

tics are best described by fractal dimensions of $3 - 1/2$ and $3 - 1/3$, respectively (Mandelbrot 1975). In the following we focus on similar questions with respect to supersonic turbulence.

In turbulence research there are several approaches to assess the flow geometry quantitatively. Indirectly, the information on fractional dimension of dissipative structures in turbulent flows can be obtained as a by-product of application of phenomenological cascade models, e.g. the hierarchical structure (HS) model developed by She & Leveque (1994) and Dubrulle (1994) for incompressible Navier-Stokes turbulence and later extended to supersonic flows by Boldyrev (2002). The HS model is based on the assumption of log-Poisson statistics for the energy dissipation rate and provides an estimate for fractal dimension, D , of the most singular structures based on the detailed knowledge of high-order *velocity* structure functions (e.g., Kritsuk & Norman 2004; Padoan et al. 2004b). While the HS model appears to reproduce experimental data quite well in a rather diverse set of applications extending far beyond the limits of the original study of fully developed turbulence (e.g., Liu et al. 2004), the uncertainty in the scaling properties of high-order velocity statistics remains large. To nail down the D value thus obtained from numerical experiments, one has to go beyond the current resolution limits to resolve the inertial subrange dynamics sufficiently well and to provide a statistical data sample of a reasonably large

size. That would reduce the effects of the statistical noise and anisotropies which tend to strongly contaminate the high-order velocity statistics (e.g., Porter et al. 2002). We leave a more detailed discussion of the HS model to a follow-up paper and focus here instead on a direct measurement of the fractal dimension of the density field using conventional techniques. Note, however, that there is no trivial physical connection between the fractal dimensions measured by these two techniques, i.e. they do not necessarily refer to the same fractal object since one is based exclusively on the velocity information, while the other is based on the density information.

For physical systems in three-dimensional space, like supersonic turbulent boxes, it is often easier to directly estimate the mass dimension that contains information about the density scaling with size. To do so, we select a sequence of box sizes $\ell_1 > \ell_2 > \dots > \ell_n$ and cover high-density peaks with concentric cubes of those linear sizes. Denoting $M(\ell_i)$ as the mass contained inside the box of size ℓ_i , one can plot $\log M(\ell_i)$ versus $\log \ell_i$ to reveal a scaling range where the points follow a straight line,

$$M(\ell) \propto \ell^{D_m}. \quad (30)$$

The slope of the line, D_m , then gives an estimate of the mass dimension for the density distribution. Note that the centers of the box hierarchies cannot be chosen arbitrarily. They must belong to the fractal set, or else, in the limit $\ell \rightarrow 0$, one would end up with boxes containing essentially no mass. In practice, we selected as centers the positions where the gas density is higher or equal to one-half of the density maximum for a given snapshot. We then determined D_m by taking an average over all centers from five statistically independent density snapshots separated from each other by roughly one dynamical time.

Figure 18 shows the mass scaling with the box size ℓ compensated by ℓ^{-2} based on the procedure described above. The slope of the mass–scale dependence breaks from roughly 2 in the dissipation-dominated range of small scales to ~ 2.4 in the inertial subrange that is free from the bottleneck effect. The transition point at $\ell \sim 30\Delta$ coincides with the break point present in all power spectra discussed above. On small scales, the geometry of the density field in supersonic turbulence is dominated by two-dimensional shock surfaces. This is where the numerical dissipation dominates in PPM.

On larger scales, where the dissipation is practically negligible, the clustered shocks form a sophisticated pattern with fractal dimension $D_m = 2.39 \pm 0.01$. Since the dynamic range of our simulations is limited, we can only reproduce this scaling in a quite narrow interval from $\sim 40\Delta$ to $\sim 160\Delta$, and thus, the actual uncertainty of our estimate for D_m in the inertial range can still be on the order of ± 0.1 or even larger. The break present in the $(\log M - \log \ell)$ relation may indicate a change in intermittency properties of turbulence at the meeting point of the inertial and dissipation ranges (see, e.g. Frisch 1995).

3.9. A Simple Compressible Cascade Model

More than half a century ago, von Weizsäcker (1951) introduced a phenomenological model for three-dimensional compressible turbulence with an intermittent, scale-invariant hierarchy of density fluctuations described by a simple equation that relates the mass density at two successive levels to the corresponding scales through a universal measure of the de-

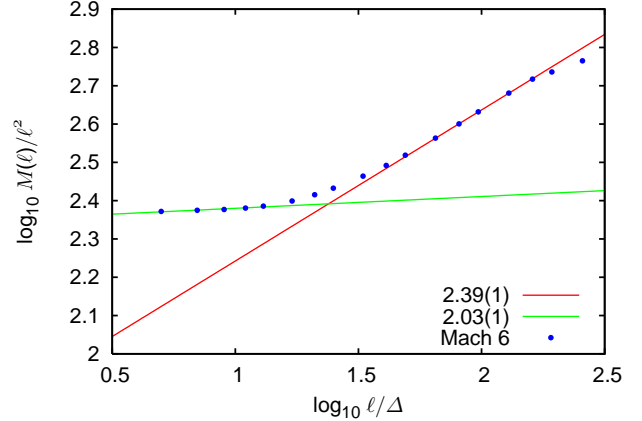


FIG. 18.— Gas mass within a box of size ℓ normalized by ℓ^2 as a function of the box size. The mass dimension D_m of the density distribution is determined by the slope of this relationship. A horizontal line would correspond to $D_m = 2$. The data points represent averages over five density snapshots. The straight lines are the least-squares fits to the data for $\log \ell/\Delta \in [0.5, 1.2]$ and $\log \ell/\Delta \in [1.7, 2]$.

gree of compression, α ,

$$\frac{\rho_\nu}{\rho_{\nu-1}} = \left(\frac{\ell_\nu}{\ell_{\nu-1}} \right)^{-3\alpha}. \quad (31)$$

The only free parameter of the model is the geometrical factor α which takes the value of 1 in a special case of isotropic compression in three dimensions, $1/3$ for a perfect one-dimensional compression, and zero in the incompressible limit.

The kinetic energy supplied to the system at large scales is being transferred through the hierarchy by nonlinear interactions. Lighthill (1955) pointed out that, in a compressible fluid, the mean volume energy transfer rate $\rho u^2 u/\ell$ is constant in a statistical steady state, so that

$$u \sim (\ell/\rho)^{1/3}. \quad (32)$$

From these two equations, assuming mass conservation, Fleck (1996) derived a set of scaling relations for the velocity, specific kinetic energy, density, and mass:⁹

$$u \sim \ell^{1/3+\alpha}, \quad (33)$$

$$\mathcal{E}(k) \sim k^{-\beta} \sim k^{-5/3-2\alpha}, \quad (34)$$

$$\rho \sim \ell^{-3\alpha}, \quad (35)$$

$$M(\ell) \sim \ell^{D_m} \sim \ell^{3-3\alpha}, \quad (36)$$

where all the exponents depend on the compression measure α . The compression measure, in turn, is a function of the rms Mach number of the turbulent flow. In the incompressible limit, $\mathcal{M} \rightarrow 0$ and $\alpha \rightarrow 0$. There are also scaling relations for $v \equiv \rho^{1/3} u$ that follow directly from equation (32) and extend the incompressible K41 velocity scaling into the compressible regime,¹⁰

$$v^p = (\rho^{1/3} u)^p \sim \ell^{p/3}. \quad (37)$$

These hint at a unique generalization of the velocity structure functions for compressible flows,

$$S_p(\ell) \equiv \langle |\mathbf{v}(\mathbf{r}+\ell) - \mathbf{v}(\mathbf{r})|^p \rangle \sim \ell^{p/3}, \quad (38)$$

⁹ Similar ideas were discussed earlier by Biglari & Diamond (1988, 1989) in a slightly different context of self-gravitating compressible fluids.

¹⁰ Note that Kolmogorov (1941a,b) and Obukhov (1941) only considered $p \leq 3$ and never went as far as to consider $p > 3$ (cf. Frisch 1995).

with $S_3 \sim \ell$ (see also the discussion in Section 3.4). The scaling laws expressed by equation (38) should not necessarily be exact and, as the incompressible K41 scaling, may require “intermittency corrections” that will be addressed in detail elsewhere. Our discussion here is limited to low-order statistics ($p \leq 3$) for which the “corrections” are supposedly small. The compression measure α could also depend on the order p in addition to its Mach number dependency. However, as we show below, a linear approximation $\alpha = \text{const}$ built into this simple cascade model may prove reasonable for the low-order density and velocity statistics.

Before turning to properties of the density-weighted velocities \mathbf{v} , let us first assess the predictive power of Fleck’s model using the statistics we already derived. Since from the simulations we know the scaling of the first-order velocity structure functions, we can get an estimate of the geometric factor α for the Mach 6 flow using equation (33). Assuming the inertial range scaling, $S_1 \sim \ell^{0.54}$, we get $\alpha \approx 0.21$ and $D_m \approx 2.38$ from equation (36). This is consistent with our direct measurement of the mass dimension, $D_m \approx 2.4$, for the same range of scales.

We can also do a consistency check based on the second-order statistics. From the inertial range scaling of the second-order structure functions, we get $\mathcal{E}(k) \sim k^{-1.97}$ and therefore $\alpha = 0.15$. This value corresponds to the fractal dimension $D_m \approx 2.55$ that is higher, but still reasonably close to our direct estimate. The discrepancy can in part be attributed to a deficiency of Fleck’s model that asymptotically approaches the space-filling K41 cascade in the limit of weak compressibility ($\alpha \rightarrow 0$) and thus does not take the full account of the intermittency of the velocity field.

It is interesting to compare the interface dimension D_i introduced by Meneveau & Sreenivasan (1990) for intermittent incompressible turbulence based on the so-called Reynolds number similarity

$$D_i = 2 + \zeta_1, \quad (39)$$

where ζ_1 as before is the exponent of the first-order velocity structure function, with the mass dimension $D_m = 3 - 3\alpha$. Since both quantities characterize the same intermittent structures, they may well refer to the same fractal object in our compressible case. If one assumes $D_i = D_m = D$, keeping in mind that $\zeta_1 = 1/3 + \alpha$ as follows from (33), it is easy to compute the compression parameter $\alpha = 1/6 \approx 0.16(6)$ as well as the fractal dimension, $D = 2.5$, that appear to be in accord with the original proposal by Fleck (1996) and with the numbers listed above.

Finally, we can use the scaling exponents of the velocity power spectrum $\mathcal{E}(k) \sim k^{-1.97}$ and of the kinetic energy spectrum $E(k) \sim k^{-1.52}$ to find α from the density scaling in equation (35). We get

$$\rho \sim \frac{E(k)}{\mathcal{E}(k)} \sim k^{0.45} \sim \ell^{-3\alpha}, \quad (40)$$

and thus, $\alpha = 0.15$, consistent with the previous estimate based on the second-order statistics.

Overall, within the uncertainties, Fleck’s model appears to successfully reproduce the low-order velocity and density statistics from our numerical simulations and supports our direct measurement of the mass dimension D_m as well.

Let us now check how well equation (37) is satisfied in our simulations by computing the power spectrum $\Sigma(k)$ of the density-weighted velocity \mathbf{v} as a $p = 2$ diagnostic. We define $\Sigma(k)$ in exactly the same way as $\mathcal{E}(k)$ was defined in Section 3.3, but substitute \mathbf{v} in place of the velocity \mathbf{u} . As

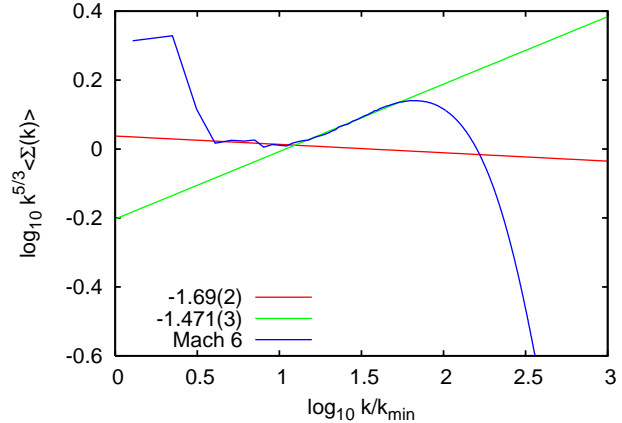


FIG. 19.— Time-averaged power spectrum of the density-weighted velocity $\mathbf{v} \equiv \rho^{1/3}\mathbf{u}$ compensated by $k^{5/3}$. The straight lines represent the least-squares fits to the data for $\log k/k_{\min} \in [0.5, 1.1]$ and $\log k/k_{\min} \in [1.2, 1.8]$. The inertial subrange slope is in excellent agreement with the model prediction.

can be seen from Figure 19, the inertial range power index, $\beta = 1.69 \pm 0.02$, is very close to the Kolmogorov value of $5/3$.

To further check our conjecture expressed by equation 38, we measured the first three scaling exponents for the modified structure functions S_p using a subsample of 35 snapshots evenly distributed in time through $t \in [6, 10]t_d$ using a sample of 2×10^9 point pairs per PDF per snapshot. The resulting third-order exponents are very close to unity as expected, $\zeta_3^\perp = 1.01 \pm 0.02$ and $\zeta_3^\parallel = 0.95 \pm 0.02$. This strongly suggests that a relationship similar to Kolmogorov’s “4/5” law may hold for compressible flows as well.

Both the first-order exponents $\zeta_1^\perp = 0.467 \pm 0.004$ and $\zeta_1^\parallel = 0.451 \pm 0.004$ and the second-order exponents $\zeta_2^\perp = 0.80 \pm 0.01$ and $\zeta_2^\parallel = 0.76 \pm 0.01$ slightly deviate from the K41 $p/3$ scaling as would be the case in intermittent turbulence. The corresponding relative (to the 3rd order) exponents $Z_1^\perp = 0.46$ and $Z_1^\parallel = 0.47$ and $Z_2^\perp = 0.79$ and $Z_2^\parallel = 0.80$ are also somewhat higher than their counterparts for the velocity structure functions discussed in Section 3.4, indicating certain structural differences between the \mathbf{u} and \mathbf{v} fields.

Note, as the Mach number changes from $\mathcal{M} < 1$ to $\mathcal{M} = 6$, the slope of the density power spectrum gets shallower from $-7/3$ to -1.1 , but the slope of the velocity power spectrum gets steeper from $-5/3$ to -1.9 . At the same time, the power spectrum of the mixed variable \mathbf{v} remains approximately invariant, as predicted by the model.

Our numerical experiments thus confirm one of the basic assumptions adopted in the compressible cascade model, namely, that equation (32) for the energy transfer rate holds true. The first assumption concerning the properties of the self-similar hierarchical density structure, equation (31) put forward by von Weizsäcker (1951), seems to be also satisfied in the simulations quite well, at least to the first order.

4. DISCUSSION

The major deficiency of the numerical experiments discussed above is still their limited spatial resolution that bounds the integral scale Reynolds numbers to values much smaller than those estimated for the real molecular clouds. This hurdle apparently cannot be overcome in the near future, but still the progress achieved in the past 15 years in this direction is very impressive.

The second important deficiency of our model is the lack of magnetic effects which are known to be essential for star formation applications. This subject still remains a topic for the future work awaiting the development of a high-quality MHD solver suitable to modeling of supersonic flows at moderately high Reynolds numbers with computational resources available today.

Another set of potential issues relates to the external driving force that is supposed to simulate the energy input by HD instabilities in real molecular clouds. The large-scale driving force we used in these simulations is not perfectly isotropic due to the uneven distribution of power between the solenoidal and dilatational modes (perhaps, a typical situation for the interstellar conditions). We also use a *static* driving force that could potentially cause some anomalies on timescales of many dynamical times. However, while strong anisotropies can significantly affect the scaling of high-order moments (Porter et al. 2002; Mininni et al. 2006), the departures from Kolmogorov-like scaling we observe in the lower order statistics appear to be too strong to be explained solely as a result of the specific properties of the driving. The sensitivity of our result to turbulence forcing remains to be verified with future high-resolution simulations involving a variety of driving options.

The options for observational validation of our numerical models are limited. Interstellar turbulence in general and supersonic turbulence in molecular clouds in particular could hardly be uniform and/or isotropic (Kaplan & Pikelner 1970). There are multiple driving mechanisms of different natures operating on different scales in the ISM (Norman & Ferrara 1996; Mac Low & Klessen 2004), so the source function of turbulence is expected to be broadband. Various observational techniques employed to extract information about the scaling properties of turbulence have their own limitations, including a finite instrumental resolution, insufficiently large data sets, inability to fully access the three-dimensional information without additional a priori assumptions, etc. Moreover, complexity of the effective equation of state of the ISM and many other physical processes so far ignored in the simplified numerical models should also make the comparison of observations and simulations uncertain. Nevertheless, it makes sense to compare our results with the scaling properties of supersonic turbulence obtained from observations.

Applying the velocity channel analysis (VCA) technique (Lazarian & Pogosyan 2000, 2006) to power spectra of integrated intensity maps and single-velocity channel maps of the Perseus region, Padoan et al. (2006) found a velocity power spectrum index $\beta = 1.8$ that is reasonably close to our measurement $\beta = 1.95$. The structure function exponents measured for the M1-67 nebula by Grosdidier et al. (2001), $\zeta_1 \approx 0.5$ and $\zeta_2 \approx 0.9$, match quite nicely with our results discussed in Section 3.4, $\zeta_1 = 0.54$ and $\zeta_2 = 0.97$.

Using maps of the $^{13}\text{CO } J = 1 - 0$ emission line of the molecular cloud complexes in Perseus, Taurus, and Rosetta, Padoan et al. (2004a) computed the power spectra of the column density estimated using the LTE¹¹ method (Dickman 1978). The slopes of the measured spectra corrected for temperature and saturation effects on the $^{13}\text{CO } J = 1 - 0$ line, -0.74 ± 0.07 , -0.74 ± 0.08 , and -0.76 ± 0.08 , respectively, are notably shallower than our estimate for the density spectrum power index -1.07 ± 0.01 (see Section 3.6). The apparent 4σ discrepancy is most probably due to an insufficiently

high Mach number adopted in our simulations. Alternatively, it can be attributed to anisotropies in the molecular cloud turbulence, intermittent large-scale driving force acting on the clouds, or limitations of the LTE method.

As far as the fractal dimension is concerned, the observational measurements for molecular clouds and star-forming regions tend to cluster around $D = 2.3 \pm 0.3$ (Elmegreen & Falgarone 1996; Elmegreen & Elmegreen 2001). Stochastically variable turbulent [WC] winds from “dustars” feeding the ISM also demonstrate similar fractal dimension $D = 2.2 - 2.3$, and the same morphology of clumps forming and dissipating in real time is clearly seen in the outer parts of the wind where the picture is not smeared by projection effects (Grosdidier et al. 2001).

5. CONCLUSIONS

Using large-scale numerical simulations of nonmagnetic highly compressible driven turbulence at an rms Mach number of 6, we were able to resolve the inertial range scaling and have demonstrated that:

1. The probability density function of the gas density is perfectly represented by a lognormal distribution over many decades in probability as predicted from simple theoretical considerations.
2. Low-order *velocity* statistics deviate substantially from Kolmogorov laws for incompressible turbulence. Both velocity power spectra and velocity structure functions show steeper than Kolmogorov slopes, with the scaling exponents of the third-order velocity structure functions far in excess of unity.
3. The *density* power spectrum is instead substantially shallower than in weakly compressible turbulent flows.
4. The *kinetic energy* power spectrum (built on $\mathbf{w} \equiv \sqrt{\rho}\mathbf{u}$) is shallower than Kolmogorov’s 5/3-law. The power spectra for both the solenoidal and the dilatational parts of \mathbf{w} obtained through Helmholtz decomposition ($\mathbf{w} = \mathbf{w}_S + \mathbf{w}_D$) have the same slopes as the total kinetic energy spectrum pointing to the unique energy cascade captured by $E(k)$; their shares in the total energy balance are 68% and 32%, respectively.
5. As should have been expected, the mean volume energy transfer rate in compressible turbulent flows, $\rho u^2 u/\ell$, is very close to constant in a (statistical) steady state. Our simulations show that the power spectrum of $\mathbf{v} \equiv \rho^{1/3}\mathbf{u}$ scales approximately as $k^{-5/3}$ and the third order structure function of \mathbf{v} scales linearly with ℓ in the inertial range.
6. The directly measured mass dimension of the “fractal” density distribution is about 2.4 in the inertial range and 2.0 in the dissipation range. The geometry of supersonic turbulence is dominated by clustered corrugated shock fronts.

These results strongly suggest that the Kolmogorov laws originally derived for incompressible turbulence would also hold for highly compressible flows as soon as they are extended by replacing the pure velocity statistics with statistics of mixed quantities, such as the density-weighted fluid velocity $\mathbf{v} \equiv \rho^{1/3}\mathbf{u}$.

¹¹ Local thermodynamic equilibrium.

Both the scaling properties and the geometry of supersonic turbulence we find in our numerical experiments support a phenomenological description of intermittent energy cascade in a compressible turbulent fluid and suggest a reformulation of inertial range intermittency models for compressible turbulence in terms of the proposed extension to the K41 theory.

The scaling exponents of the velocity diagnostics, the morphology of turbulent structures, and the fractal dimension of the mass distribution determined in our numerical experiments demonstrate good agreement with the corresponding observed quantities in supersonically turbulent molecular clouds and line radiation-driven winds from carbon-sequence

Wolf-Rayet stars.

We are grateful to Åke Nordlund who kindly provided us with his OpenMP-parallel routines to compute the power spectra. This research was partially supported by NASA ATP grant NNG05-6601G, NSF grants AST 05-07768 and AST 06-07675, and NRAC allocation MCA098020S. We utilized computing resources provided by the San Diego Supercomputer Center and the National Center for Supercomputer Applications.

REFERENCES

- Acker, A., Gesicki, K., Grosdidier, Y., & Durand, S. 2002, *A&A*, 384, 620
 Armi, L., & Flament, P. 1985, *J. Geophys. Research*, 90, 11779
 Armstrong, J. W., Rickett, B. J., & Spangler, S. R. 1995, *ApJ*, 443, 209
 Baty, H., Keppens, R., & Comte, P. 2003, *Physics of Plasmas*, 10, 4661
 Bayly, B. J., Levermore, C. D., & Passot, T. 1992, *Phys. Fluids*, 4, 945
 Benzi, R., Biferale, L., Ciliberto, S., Struglia, M.V., Tripiccion, R. 1996, *Physica D*, 96, 162
 Benzi, R., Ciliberto, S., Tripiccion, R., Baudet, C., Massaioli, F., Succi, S. 1993, *Phys. Rev. E*, 48, R29
 Biglari, H., & Diamond, P. H. 1988, *Phys. Rev. Lett.*, 61, 1716
 Biglari, H., & Diamond, P. H. 1989, *Physica D Nonlinear Phenomena*, 37, 206
 Biskamp, D. 2003, *Magnetohydrodynamic Turbulence* (Cambridge: Cambridge University Press)
 Boldyrev, S. 2002, *ApJ*, 569, 841
 Boldyrev, S., Nordlund, Å., & Padoan, P. 2002, *ApJ*, 573, 678
 Brunt, C. M. 2003, *ApJ*, 584, 293
 Brunt, C. M., Heyer, M. H., Vázquez-Semadeni, E., & Pichardo, B. 2003, *ApJ*, 595, 824
 Colella, P. & Woodward, P. R. 1984, *J. Comput. Phys.*, 54, 174
 Davidson, P. A., & Pearson, B. R. 2005, *Phys. Rev. Lett.*, 95, 214501
 de Kármán, T., & Howarth, L. 1938, *Proc. R. Soc. Lond. A*, 164, 192
 Dickman, R. L. 1978, *ApJS*, 37, 407
 Dobler, W., Haugen, N. E., Yousef, T. A., & Brandenburg, A. 2003, *Phys. Rev. E*, 68, 026304
 Dubrulle, B. 1994, *Phys. Rev. Lett.*, 73, 959
 Elmegreen, B. G., & Elmegreen, D. M. 2001, *AJ*, 121, 1507
 Elmegreen, B. G., & Falgarone, E. 1996, *ApJ*, 471, 816
 Elmegreen, B. G., & Scalo, J. 2004, *ARA&A*, 42, 211
 Falkovich, G. 1994, *Phys. Fluids*, 6, 1411
 Fleck, R. C., Jr. 1996, *ApJ*, 458, 739
 Frisch, U. 1995, *Turbulence: the legacy of A. N. Kolmogorov* (Cambridge: Cambridge University Press)
 Frisch, U., Bec, J. 2001, *Burgulence*, in *Les Houches 2000: New Trends in Turbulence*, ed. M. Lesieur, A. Yaglom, and F. David (Berlin: Springer), 341
 Gaffet, B. 1985, *J. Fluid Mech.*, 156, 141
 Grosdidier, Y., Moffat, A. F. J., Blais-Ouellette, S., Joncas, G., & Acker, A. 2001, *ApJ*, 562, 753
 Haugen, N. E. & Brandenburg, A. 2004, *Phys. Rev. E*, 70, 026405
 Heitsch, F., Burkert, A., Hartmann, L. W., Slyz, A. D., & Devriendt, J. E. G. 2005, *ApJL*, 633, L113
 Helmholtz, H. 1868, *Monasber. Berlin Akad.*, 215
 Kaneda, Y., Ishihara, T., Yokokawa, M., Itakura, K., & Uno, A. 2003, *Phys. Fluids*, 15, L21
 Kaplan, S. A., & Pikelner, S. B. 1970, *The Interstellar Medium* (Cambridge: Harvard University Press)
 Kaplan, S. A. & Pronik, V. I. 1953, *Dokl. Akad. Nauk SSSR*, 89, 643
 Keppens, R., Tóth, G., Westermann, R. H. J., & Goedbloed, J. P. 1999, *J. Plasma Phys.*, 61, 1
 Kida, S. & Orszag, S. A. 1990, *J. Sci. Comput.*, 5, 85
 ——. 1992, *J. Sci. Comput.*, 7, 1
 Kim, J. & Ryu, D. 2005, *ApJL*, 630, L45
 Kolmogorov, A. N. 1941a, *Dokl. Akad. Nauk SSSR*, 30, 299
 ——. 1941b, *Dokl. Akad. Nauk SSSR*, 31, 538
 ——. 1941c, *Dokl. Akad. Nauk SSSR*, 32, 19
 ——. 1962, *J. Fluid Mech.*, 13, 82
 Kornreich, P., & Scalo, J. 2000, *ApJ*, 531, 366
 Kritsuk, A. G., & Norman, M. L. 2004, *ApJL*, 601, L55
 Kritsuk, A. G., Norman, M. L., & Padoan, P. 2006, *ApJL*, 638, L25
 Larson, R. B. 1981, *MNRAS*, 194, 809
 Lazarian, A., & Pogosyan, D. 2000, *ApJ*, 537, 720
 ——. 2006, *ApJ*, 652, 1348
 Lele, S. K. 1994, *Ann. Rev. Fluid Mech.*, 26, 211
 Li, P. S., Norman, M. L., Mac Low, M.-M., & Heitsch, F. 2004, *ApJ*, 605, 800
 Lighthill, M. J. 1955, in *IAU Symp. 2: Gas Dynamics of Cosmic Clouds* (Amsterdam: North Holland), 121
 Liu, J., She, Z.-S., Guo, H., Li, L., & Ouyang, Q. 2004, *Phys. Rev. E*, 70, 036215
 Mac Low, M.-M., & Klessen, R. S. 2004, *Rev. Mod. Phys.*, 76, 125
 Mandelbrot, B. B. 1974, *J. Fluid Mech.*, 62, 331
 ——. 1975, *J. Fluid Mech.*, 72, 401
 Meneveau, C., & Sreenivasan, K. R. 1990, *Phys. Rev. A*, 41, 2246
 Miles, J. W. 1957, *J. Fluid Mech.*, 3, 185
 Mininni, P. D., Alexakis, A., & Pouquet, A. 2006, *Phys. Rev. E*, 74, 016303
 Miura, A., & Pritchett, P. L. 1982, *J. Geophys. Research*, 87, 7431
 Monin, A. S., & Yaglom, A. M. 1975, *Statistical Fluid Mechanics; Mechanics of Turbulence*, Vol. 2 (Cambridge, MA: MIT Press)
 Moyal, J. E. 1951, *Proc. Cambridge Philos. Soc.*, 48, 329
 Nordlund, Å. K. & Padoan, P. 1999, in *Interstellar Turbulence*, eds. J. Franco & A. Carraminana, 218
 Norman, C. A., & Ferrara, A. 1996, *ApJ*, 467, 280
 Obukhov, A. M. 1941, *Dokl. Akad. Nauk SSSR*, 32, 22
 ——. 1962, *J. Fluid Mech.*, 13, 77
 Padoan, P., Jimenez, R., Juvela, M., & Nordlund, Å. 2004a, *ApJL*, 604, L49
 Padoan, P., Jimenez, R., Nordlund, Å., & Boldyrev, S. 2004b, *Phys. Rev. Lett.*, 92, 191102
 Padoan, P., Juvela, M., Kritsuk, A., & Norman, M. L. 2006, *ApJL*, 653, L125
 Padoan, P., & Nordlund, A. 1997, *astro-ph/9706176*
 ——. 1999, *ApJ*, 526, 279
 ——. 2002, *ApJ*, 576, 870
 Padoan, P., Nordlund, Å., & Jones, B. J. T. 1997, *MNRAS*, 288, 145
 Padoan, P., Nordlund, A., Kritsuk, A. G., Norman, M. L., & Li, P. S. 2007, *ApJ*, 661, 972
 Passot, T., Pouquet, A., & Woodward, P. 1988, *A&A*, 197, 228
 Passot, T. & Vázquez-Semadeni, E. 1998, *Phys. Rev. E*, 58, 4501
 Politano, H., Pouquet, A. 1998, *Geophys. Res. Lett.*, 25, 273
 Porter, D. H., Pouquet, A., Sytine, I., & Woodward, P. 1999, *Physica A*, 263, 263
 Porter, D. H., Pouquet, A., & Woodward, P. R. 1992a, *Theor. Comput. Fluid Dyn.*, 4, 13
 ——. 1992b, *Phys. Rev. Lett.*, 68, 3156
 ——. 1994, *Phys. Fluids*, 6, 2133
 ——. 2002, *Phys. Rev. E*, 66, 026301
 Porter, D. H., & Woodward, P. R. 1994, *ApJS*, 93, 309
 Porter, D. H., Woodward, P. R., & Pouquet, A. 1998, *Phys. Fluids*, 10, 237
 Pouquet, A., Passot, T., & Leorat, J. 1991, in *IAU Symp. 147, Fragmentation of Molecular Clouds and Star Formation*, ed. E. Falgarone, F. Boulanger, & G. Duvert (Dordrecht: Kluwer), 101
 Ryu, D., Jones, T. W., & Frank, A. 2000, *ApJ*, 545, 475
 Samtaney, R., Pullin, D. I., & Kosovic, B. 2001, *Phys. Fluids*, 13, 1415
 She, Z.-S., & Leveque, E. 1994, *Phys. Rev. Lett.*, 72, 336
 She, Z.-S., & Waymire, E. C. 1995, *Phys. Rev. Lett.*, 74, 262
 Sreenivasan, K. R. & Bershadski, A. 2005, *Pramana — J. Phys.*, 64, 315
 Sytine, I. V., Porter, D. H., Woodward, P. R., Hodson, S. W., & Winkler, K.-H. 2000, *J. Comput. Phys.*, 158, 225
 Vázquez-Semadeni, E. 1994, *ApJ*, 423, 681
 Vishniac, E. T. 1994, *ApJ*, 428, 186
 von Weizsäcker, C. F. 1951, *ApJ*, 114, 165